Research in Astronomy and Astrophysics, 24:075003 (15pp), 2024 July https://doi.org/10.1088/1674-4527/ad462c

Mid-infrared Period–Luminosity Relations of Gaia DR3 Long Period Variables

Xiaohan Chen[1,2,3], Xiaodian Chen[3,4,5,6], Licai Deng[3,4,5], Shu Wang[3,5], and Tianlu Chen[1,2]
[1] Department of Physics, College of Science, Tibet University, Lhasa 850000, China; chenxh@bao.ac.cn
[2] Key Laboratory of Cosmic Rays (Tibet University), Ministry of Education, Lhasa 850000, China
[3] CAS Key Laboratory of Optical Astronomy, National Astronomical Observatories, Chinese Academy of Sciences, Beijing 100101, China; chenxiaodian@nao.cas.cn
[4] School of Astronomy and Space Science, University of the Chinese Academy of Sciences, Beijing 100049, China
[5] Department of Astronomy, China West Normal University, Nanchong 637009, China
[6] Institute for Frontiers in Astronomy and Astrophysics, Beijing Normal University, Beijing 102206, China
Received 2024 April 16; revised 2024 April 22; accepted 2024 April 29; published 2024 June 19

Abstract

Long period variable (LPV) stars are very promising distance indicators in the infrared bands. We selected asymptotic giant branch (AGB) stars in the Large and Small Magellanic Cloud (LMC and SMC) from the Gaia Data Release 3 LPV catalog, and classified them into oxygen-rich (O-rich) and carbon-rich (C-rich) AGB stars. Using the Wide-field Infrared Survey Explorer database, we determined the W1- and W2-band period–luminosity relations (PLRs) for each pulsation-mode sequence of AGB stars. The dispersion of the PLRs of O-rich AGB stars in sequences C′ and C is relatively small, around 0.14 mag. The PLRs of LMC and SMC are consistent in each sequence. In the W2 band, the PLR of large-amplitude C-rich AGB stars is steeper than that of small-amplitude C-rich AGB stars, due to their more circumstellar dust. By two methods, we find that some PLR sequences of O-rich AGB stars in the LMC are dependent on metallicity. The coefficients of the metallicity effect are $\beta = -0.533 \pm 0.213$ mag dex^{1} and $\beta = -0.767 \pm 0.158$ mag dex^{1} for sequence C in W1 and W2 bands, respectively. The significance of the metallicity effect in W1 band for the four sequences is $2.2-3.5\sigma$. Both of these imply that distance measurements using O-rich Mira may need to take the metallicity effect into account.

Key words: stars: variables: general – stars: distances – infrared: stars

1. Introduction

Long period variables (LPVs) are representatives of the asymptotic giant branch (AGB) and red giant branch (RGB) phases of the evolution of low- and intermediate-mass stars. Due to their large amplitude variations in the optical bands and pulsation periods of about 10–1000 days, LPVs are easily detectable and therefore have received much attention. In recent years, LPVs in the Milky Way, Large Magellanic Cloud (LMC), Small Magellanic Cloud (SMC) and other galaxies have been extensively searched for and studied using different databases (Menzies et al. 2019; Chen et al. 2020; Saremi et al. 2020; Groenewegen 2022; Suh 2022). The study of the period–luminosity relations (PLRs) of LPVs has developed rapidly when large microlensing surveys published long-term photometry of a large number of stars. Cook et al. (1996) first pointed out that the variable stars in the Massive Compact Halo Object experiment database for LMC present five parallel sequences in the period–luminosity (PL) diagram. Wood et al. (1999) and Wood (2000) classified them into five sequences (labeled A, B, C, D, and E). Subsequent studies classified more sequences. Ita et al. (2004) denoted an additional sequence closed to the sequence B as C′. Moreover, Wood (2015) defined the sequence A′. In the evolution model, stars entering the AGB phase are oxygen-rich (O-rich), and they can turn into carbon-rich (C-rich) objects after the dredge-up episodes. Therefore, AGB stars can be classified as O-rich and C-rich based on the relative abundance of oxygen to carbon in their surface composition. Soszyński et al. (2004) divided AGB stars in LMC and SMC into O-rich and C-rich AGB stars. Then Soszyński et al. (2005) divided Mira variables (Miras) and semi-regular variables (SRVs) in LMC into O-rich and C-rich. LPV sequences consist of Miras, SRVs, OGLE small-amplitude red giants and long secondary period (LSP) variables. Their pulsations are caused by radial and non-radial modes (Wood 2015), and therefore they follow several distinct PLRs, which make them potential distance indicators (Soszyński et al. 2007). In addition, different sequences of PLRs are associated with different pulsation models, which can be an important tool to constrain the stellar evolution (Trabucchi et al. 2017).

In the infrared bands, LPVs are as bright or brighter than Cepheids. The PLRs of LPVs have little dependence on metallicity (Goldman et al. 2019), and can be used as independent distance indicators to measure distances. The PLRs in the near-infrared and mid-infrared (MIR) bands are tighter than those in the optical bands due to the insensitivity to effective temperature and extinction (Iwanek et al. 2021a). In recent years, PLRs of LPV subtypes in the Milky Way and other galaxies have been studied in a wide range of wavelengths using different databases (Bhardwaj et al. 2019; Kudashkina 2019; Trabucchi et al. 2021). Especially for Miras, because of their tight PLRs, they can be reliable distance indicators for measuring and calibrating Galactic and extragalactic distances (Matsunaga et al. 2005; Whitelock et al. 2008; Yuan et al. 2017; Huang et al. 2018; Qin et al. 2018; Molina et al. 2019; Urago et al. 2020; Iwanek et al. 2021b). Accurate distances not only play a crucial role in understanding the formation, evolution and structure of galaxies (Iwanek et al. 2023; Parto et al. 2023), but also in measuring the Hubble constant (Huang et al. 2020).

The longer and deeper photometry of the Gaia Data Release 3 (DR3) provides a larger sample of LPVs. This work aims to study the MIR PLRs of LMC and SMC LPVs in Gaia DR3 using data from the Wide-field Infrared Survey Explorer (WISE). In Section 2, we describe the data used in this work for LPVs. In Section 3, we present some methods, including obtaining the mean magnitude in the MIR by fitting the light curves, distinguishing AGB stars from LPV candidates through the color–magnitude diagram (CMD), classifying AGB stars into O-rich and C-rich, and determining PLRs. We compare the PLRs of two galaxies and discuss the dependence of the PLR zero-points on metallicity in Section 4. This work concludes in Section 5.

2. Data

Gaia DR3's latest database covers 34 months of multi-epoch photometry, and it provides a deeper and broader search for LPVs. We selected samples from the "gaiadr3.vari_long_period_variable" catalog, which contains basic information such as pulsation frequency, amplitude, etc. for 1,720,588 LPVs. The details were described in Lebzelter et al. (2022). We then matched these sources to the Gaia DR3 main catalog "gaiadr3.gaia_source" according to the source_id to obtain other parameters such as parallax and mean magnitudes. To investigate the PLR, we removed LPVs with null values for the frequency, leaving 392,240 candidates. The frequency range is 0.00098–0.0285 day^{-1} (35–1020 days) with upper and lower limits determined by the time span and sampling mode of each LPV's observation.

In this work, we studied the LPVs in LMC and SMC separately. The Gaia database provides optical photometry. The samples of LMC and SMC LPVs were obtained by simple selection according to their spatial positions. There are 11,047 and 3045 LPVs with associated periods in the LMC ($67.^{\circ}5 < $ R.A. $< 97.^{\circ}5$, $-70^{\circ} <$ decl. $< -62^{\circ}$) and SMC ($0^{\circ} <$ R. A. $< 30^{\circ}$, $-76^{\circ} <$ decl. $< -70^{\circ}$), respectively.

The MIR PLRs of AGB stars have a smaller dispersion compared to optical PLRs. Here we used the WISE database, which provides multi-epoch MIR bands photometry. The main mission of WISE (AllWISE) was to observe the entire sky in four bands W1, W2, W3, W4. After this mission ended in 2010, observations in W1 and W2 bands were started in 2011 as part of the Near Earth Object WISE Reactivation Mission (NEOWISE-R). In order to combine AllWISE and NEOWISE-R to compose data with a longer time span, we only use the W1 and W2 bands in this work.

For LMC and SMC LPVs, we searched for counterparts within $1''$ around the Gaia coordinates and downloaded photometry in the W1 and W2 bands from the AllWISE multi-epoch photometry table, and the NEOWISE-R single exposure source table using NASA/IPAC Infrared Science Archive.[7]

Since the angular resolution of WISE ($6''$ in W1) is worse than that of Gaia, we estimated a blending factor to exclude LPVs that are blended by bright neighbors. We obtained counterparts in the $6''$ radius around the LPV in the 2MASS database and used the ratio (1.05) of total K-band flux of all sources within a $6''$ radius around the LPV to the LPV's K-band flux as a blending factor. If a blending factor of 1.1 is used, the sample size increases by only about 2%, which has little effect on the PLR fit. Therefore, a more stringent criterion (1.05) is appropriate. For these remaining sources, we added an error $\frac{\text{blending factor} - 1}{3}$ to the absolute magnitude error. Finally, 9774 and 2778 LPVs remained from the LMC and SMC, respectively.

3. Methods

3.1. Mean Magnitudes in MIR

In Section 2, we obtained the WISE W1- and W2-bands photometric data for LPVs in LMC and SMC. To optimize the MIR PLRs, we fitted the light curve with a nonlinear least squares method to measure the mean magnitude and amplitude of each LPV. First, we converted the Modified Julian Date of each WISE photometry into phase based on the LPV's period in the Gaia DR3. We then performed the fit using a sinusoidal function $m = a_0 + a_1 \cos(2\pi x) + a_2 \sin(2\pi x)$. x is the phase, a_0 is the mean magnitude and $\sqrt{a_1^2 + a_2^2}$ is the amplitude. Considering the photometric accuracy and sampling pattern of WISE, we did not use high-order functions to avoid overfitting. The number of photometry measurements from NEOWISE-R is eight times more than that from AllWISE. To obtain better mean magnitudes, we removed the LMC and SMC LPVs with NEOWISE-R photometry less than 200 and 50, respectively. We finally obtained MIR mean magnitudes of 9365 LMC and 2682 SMC LPVs.

3.2. Period–Luminosity Diagrams

LPVs can be divided into AGB stars, red supergiant (RSG) stars, and RGB stars according to their locations on the CMDs. The CMDs of LPVs in LMC and SMC are shown in Figure 1,

[7] https://irsa.ipac.caltech.edu

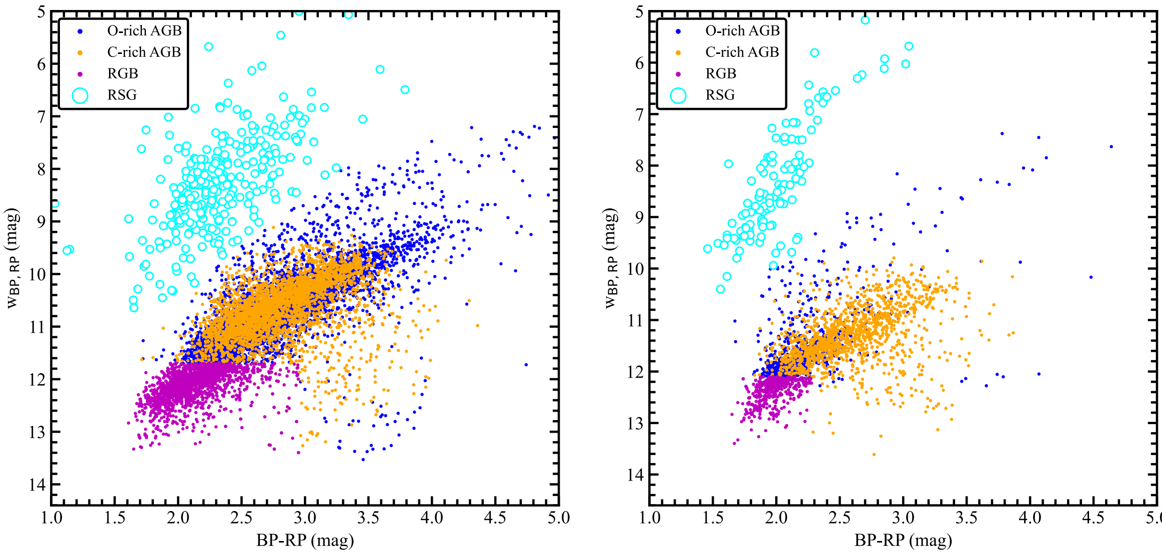

Figure 1. CMDs of LPVs in LMC (left) and SMC (right). LPVs are divided into RGB (magenta) stars, RSG (cyan) stars and AGB stars according to their location on the CMDs. AGB stars are further distinguished as O-rich (blue) and C-rich (orange) based on the parameter in the Gaia catalog.

in which we used $G_{\rm BP} - G_{\rm RP}$ and the Wesenheit indices $W_{G,{\rm BP,RP}} = G_{\rm RP} - 1.3(G_{\rm BP} - G_{\rm RP})$ as the color and the magnitude, respectively. In LPVs, RGB stars are the faintest members, and the tip of the RGB (TRGB) is their boundary with the AGB stars in absolute magnitude (Freedman et al. 2019). Boyer et al. (2011) determined the TRGB apparent magnitudes in the Spitzer [3.6] band to be 11.9 mag and 12.6 mag in LMC and SMC, respectively. In this work, we used the apparent TRGB Wesenheit magnitudes of 11.7 mag and 12.1 mag for LMC and SMC, respectively, which were determined by visual inspection. We checked that a small adjustment in TRGB magnitude has little effect on the final PLR. For example, an increase of 0.1 mag increases the number of LMC O-rich AGB stars by only 4%, and the bias in the zero-point of PLR is around or less than 0.01 mag for each sequence. We selected the RGB stars of LMC and SMC by the criteria of $W_{G,{\rm BP,RP}} \geqslant 11.7$ and $(G_{\rm BP} - G_{\rm RP}) \leqslant 2.9$ and $W_{\rm BP,RP} \geqslant 12.1$ and $(G_{\rm BP} - G_{\rm RP}) \leqslant 2.3$, respectively. For the LMC and SMC, the parallaxes of the samples conform to a Gaussian distribution, with about 1% and 2% of samples having parallaxes larger than $0\rlap{.}''2$. Therefore, the contamination of foreground stars is too small to be considered. After the selection of RGB and RSG stars, the remaining LPVs are AGB stars, which include O-rich and C-rich AGB stars.

We mainly focused on PLRs of AGB stars in this work. AGB stars are considered to be classified into O-rich and C-rich AGB stars based on their chemical abundance. As with Gaia DR2 (Mowlavi et al. 2018), the Gaia DR3 LPV catalog provides the parameter "medin_delta_wl_rp" to classify C-rich and O-rich (M-type) AGB stars, which is the median value of the pseudo-wavelength difference between the two highest peaks in the RP-spectrum of each LPV. LPV with medin_delta_wl_rp > 7 and <7 are classified as C-rich stars and O-rich stars, respectively. Notably, S-type stars are significantly enhanced in ^{12}C and s-process elements due to the third dredge-up. Although their optical spectra are still dominated by TiO, they are identified by the presence of the ZrO bands in that wavelength range (Van Eck et al. 2017). S-type stars form a kind of continuum from M- to C-type with subtypes MS, S, SC, and CS. In the Gaia catalog, the O-rich stars cover the majority of S-type stars, and a few S-type stars are included in C-rich stars (Lebzelter et al. 2022). In LMC LPVs, about 48.7% are O-rich AGB stars and 33.5% are C-rich AGB stars. The ratio of C- to O-rich AGB stars is ~0.69, which is consistent with the results of 0.61 obtained by Spano et al. (2011) and 0.63−0.72 obtained by Wiśniewski et al. (2011); 34.2% of O-rich AGB stars and 52.0% of C-rich AGB stars are found in SMC's LPVs. The proportions of O-rich and C-rich AGB stars are consistent with Mowlavi et al. (2019), and the main reason for the different proportions in LMC and SMC is their different metallicities. As the metallicity increases, efficiency of the third dredge-up decreases, leading to an increase in the oxygen abundance in the envelope of AGB stars (Mowlavi et al. 2019).

Combining the mean magnitudes in the W1 and W2 bands and the pulsation periods from the Gaia database, we plotted MIR PLR diagrams of O-rich and C-rich AGB stars in LMC and SMC. In LMC's PLR diagram (left panel of Figure 2), it is clear to see four sequences (B_o, C_o', C_o, D_o) of O-rich AGB stars and three sequences (C_c', C_c, D_c) of C-rich AGB stars. The subscripts c and o indicate that they belong to C-rich AGB stars and O-rich AGB stars, respectively. Similarly, in the SMC's

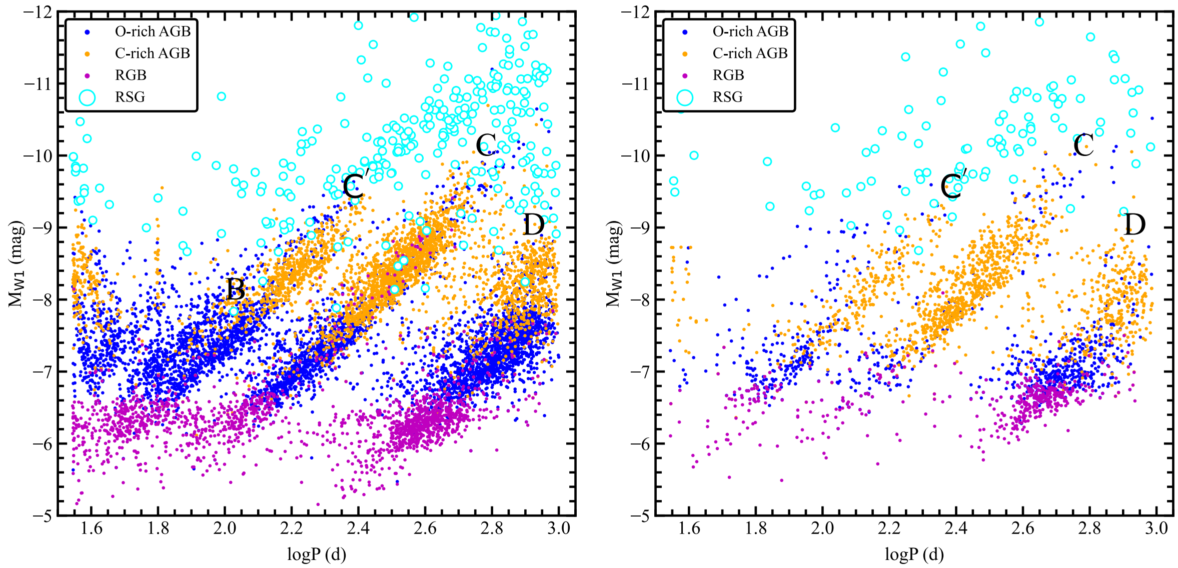

Figure 2. PL diagrams in the WISE W1 band of LPVs from LMC (left panel) and SMC (right panel). The absolute magnitudes are determined by using the distance moduli $\mu_{\mathrm{LMC}} = 18.49$ mag and $\mu_{\mathrm{SMC}} = 18.96$ mag from de Grijs et al. (2017). The colors of each subtype are the same as in Figure 1. In each panel, the pulsation sequences of AGB stars are labeled according to their location on the PL diagrams.

PLR diagram (Figure 2, right panel), there are three sequences (C_o', C_o, D_o, C_c', C_c, D_c) for both O-rich AGB stars and C-rich AGB stars. The PLR diagram in the W2 band exhibits the same multiple sequences as that in the W1 band, and we also determine the PLRs in the W2 band in the next subsection. On the MIR-band PLR diagrams, we found that the C- and O-rich AGB stars in the same sequence (e.g., C_o and C_c of the LMC AGB stars in the C sequence in the left panel of Figure 2) appear to satisfy a consistent PLR. But for Wesenheit indices $W_{\mathrm{G,BP,RP}}$, C- and O-rich AGB stars have quite different PLRs for each sequence. Therefore, we discuss the PLRs of C- and O-rich AGB stars separately.

3.3. MIR Period–Luminosity Relations

We obtained a linear PLR $M_{\mathrm{fit}} = a \times (\log P - \log P_0) + b$ for each sequence in Figure 2 through the following steps, where the $\log P_0$ is the mean logarithmic period of samples for each sequence. First, based on the PLR density maps of O-rich or C-rich AGB stars of LMC and SMC in W1 band (Figure 3), we determined the approximate boundary of period for each sequence (only considering the dense region of each sequence). We listed the period range of each sequence we used in Tables 1 and 2. In particular, the sequences B and C′ of LMC O-rich AGB stars are too close to be divided according to their period distributions, so we roughly separate them using a boundary in the M_{W1} versus $\log P$ diagram (the red line K connected by two saddle points in Figure 3). The raw samples for each sequence in the W2 band are the same as those in the W1 band. Then, we performed a linear fit to each cut sequence using the weighted least squares method with a sigma-clipping procedure. The weights are estimated by the inverse of W, where $W = \sigma_{\mathrm{M}}^2 + \sigma^2$. σ_{M} represents the absolute magnitude uncertainty that comes from the mean magnitude error in fitting light curves (σ_{m}), the uncertainty from the period (σ_{p}, we considered a period error of 10%), and the uncertainty from the blending σ_{b}. The period error will broaden the x-axis, and we converted it to the error of the absolute magnitude by the slope of PLRs, which contributes errors of around 0.15 mag. σ is the intrinsic PLR scatter; we adopted 0.10 mag because even PLRs as good as Cepheids have an intrinsic dispersion of 0.06−0.10 mag. Error in the period and error in the intrinsic dispersion of the PLR are the main terms. We performed multiple sigma-clipping until the PLR converged. Due to the small and scattered sample (see Figure 3), we used a 2σ-clipping procedure for the O-rich AGB stars in the SMC, while a 2.5σ-clipping procedure was applied for the other AGB stars.

Figures 4 and 5 present the fitting result of each sequence for the AGB stars in LMC and SMC. Through the sigma-clipping procedure, for most sequences (e.g., sequence C in Figure 4 and Figure 5), the rejected points are distributed on both sides of the high-density region used to fit the PLR and show parallel sequences. Inspection revealed that most of these points were samples from other sequences. Specifically, sequence B and sequence C′ of the LMC O-rich AGB stars are divided by a set line (K in Figure 3). This is the reason why the rejected points appear on one side (top two rows of Figure 4(a)). Linear PLRs with uncertainties for LMC and SMC sequences are listed in Tables 1 and 2, respectively. We also list the period range of

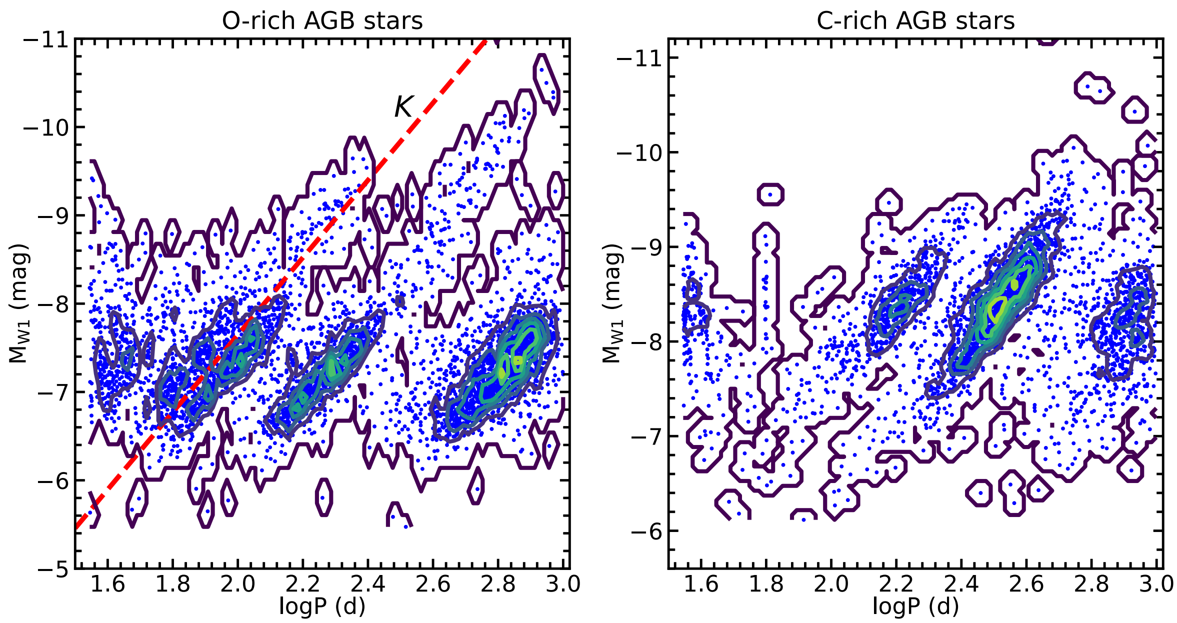

(a) LMC

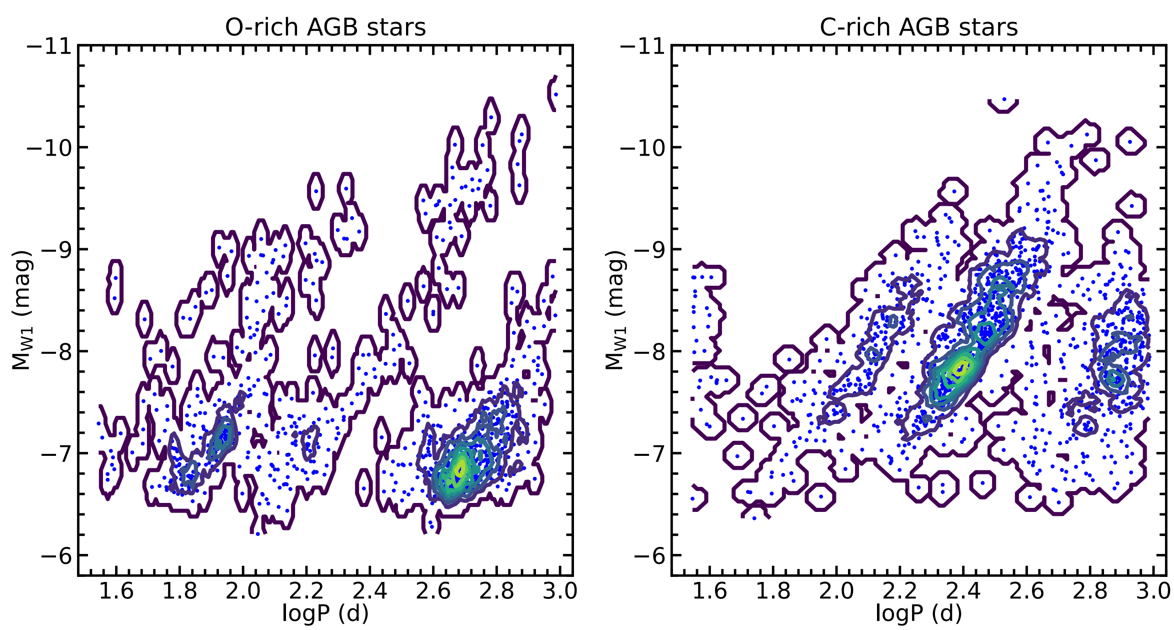

(b) SMC

Figure 3. The PL density maps of O-rich and C-rich AGB stars in LMC (a) and SMC (b) in W1 band. The red dashed line (K in left column of panel (a)) represents the boundary of adjacent sequences B_o and C'_o of LMC O-rich AGB stars.

each sequence in these tables. Among these PLRs, the PLRs of O-rich AGB stars have smaller dispersion, especially for sequences C′ and C. This suggests that these O-rich AGB stars are suitable for distance measurements. The period of sequence D is the LSP of AGB stars, and the PLR scatter of sequence D is larger than other sequences.

The histogram of the magnitude residuals relative to the PLR fit line of each sequence is shown in Figure 6. We used the Kolmogorov–Smirnov test to check the distribution and found that most of the sequences satisfy a Gaussian distribution (with a *p*-value $>$ 0.05). Sequences B and C′ of LMC's O-rich AGB stars were divided by a given line (K in Figure 3), so the stars with

Table 1
MIR PLRs for O-rich and C-rich AGB Stars in LMC

Sequence	λ	$\log P_0$	a	b	$\sigma_{\rm fit}$
		O-rich AGB stars			
B ($1.7 \leqslant \log P \leqslant 2.15$)	W1	1.877	-3.851 ± 0.085	-7.419 ± 0.008	0.197
C′ ($1.7 \leqslant \log P \leqslant 2.15$)	W1	1.973	-4.061 ± 0.057	-7.251 ± 0.005	0.129
C ($2.1 \leqslant \log P \leqslant 2.6$)	W1	2.283	-3.684 ± 0.055	-7.247 ± 0.006	0.162
D ($2.5 \leqslant \log P \leqslant 3.0$)	W1	2.800	-2.678 ± 0.064	-7.226 ± 0.006	0.252
B ($1.7 \leqslant \log P \leqslant 2.15$)	W2	1.876	-3.713 ± 0.082	-7.294 ± 0.008	0.192
C′ ($1.7 \leqslant \log P \leqslant 2.15$)	W2	1.974	-3.914 ± 0.050	-7.219 ± 0.005	0.112
C ($2.1 \leqslant \log P \leqslant 2.6$)	W2	2.276	-3.445 ± 0.062	-7.337 ± 0.006	0.185
D ($2.5 \leqslant \log P \leqslant 3.0$)	W2	2.799	-2.386 ± 0.068	-7.160 ± 0.007	0.275
		C-rich AGB stars			
C′($1.9 \leqslant \log P \leqslant 2.35$)	W1	2.183	-3.262 ± 0.087	-8.308 ± 0.009	0.199
C($2.35 \leqslant \log P \leqslant 2.8$)	W1	2.532	-4.201 ± 0.067	-8.465 ± 0.006	0.223
D($2.8 \leqslant \log P \leqslant 3.0$)	W1	2.904	-1.702 ± 0.318	-8.156 ± 0.017	0.382
C′($1.9 \leqslant \log P \leqslant 2.35$)	W2	2.184	-3.522 ± 0.089	-8.270 ± 0.009	0.202
C($2.35 \leqslant \log P \leqslant 2.8$)	W2	2.528	-4.513 ± 0.106	-8.589 ± 0.010	0.354
D($2.8 \leqslant \log P \leqslant 3.0$)	W2	2.904	-2.067 ± 0.353	-8.162 ± 0.018	0.421

Note. The PLR slope a and the zero-point b are determined from the linear fit based on $M_{\rm fit} = a \times (\log P - \log P_0) + b$, where $\log P_0$ is the mean logarithmic period of AGB stars for each sequence. $\sigma_{\rm fit}$ means the 1σ scatter in the PLR.

Table 2
MIR PLRs for O-rich and C-rich AGB Stars in SMC

Sequence	λ	$\log P_0$	a	b	$\sigma_{\rm fit}$
		O-rich AGB stars			
C′ ($1.7 \leqslant \log P \leqslant 2.05$)	W1	1.894	-3.168 ± 0.145	-7.042 ± 0.010	0.120
C ($2.02 \leqslant \log P \leqslant 2.5$)	W1	2.212	-3.011 ± 0.177	-7.141 ± 0.020	0.187
D ($2.6 \leqslant \log P \leqslant 3.0$)	W1	2.725	-2.317 ± 0.116	-6.947 ± 0.008	0.165
C′ ($1.7 \leqslant \log P \leqslant 2.05$)	W2	1.888	-2.824 ± 0.119	-6.967 ± 0.008	0.093
C ($2.02 \leqslant \log P \leqslant 2.5$)	W2	2.199	-3.292 ± 0.174	-7.133 ± 0.018	0.167
D ($2.6 \leqslant \log P \leqslant 3.0$)	W2	2.725	-1.932 ± 0.118	-6.891 ± 0.009	0.169
		C-rich AGB stars			
C′ ($1.8 \leqslant \log P \leqslant 2.23$)	W1	2.075	-3.761 ± 0.156	-7.886 ± 0.016	0.216
C ($2.2 \leqslant \log P \leqslant 2.7$)	W1	2.438	-4.290 ± 0.091	-8.168 ± 0.010	0.257
D ($2.65 \leqslant \log P \leqslant 3.0$)	W1	2.857	-2.192 ± 0.320	-7.860 ± 0.025	0.462
C′ ($1.8 \leqslant \log P \leqslant 2.23$)	W2	2.073	-3.898 ± 0.167	-7.855 ± 0.017	0.234
C ($2.2 \leqslant \log P \leqslant 2.7$)	W2	2.425	-4.308 ± 0.091	-8.080 ± 0.010	0.229
D ($2.65 \leqslant \log P \leqslant 3.0$)	W2	2.858	-2.511 ± 0.353	-7.857 ± 0.027	0.503

Note. The PLR slope a and the zero-point b are determined from the liner fit based on $M_{\rm fit} = a \times (log\ P - \log P_0) + b$, where $\log P_0$ is the mean logarithmic period of AGB stars for each sequence. $\sigma_{\rm fit}$ means the 1σ scatter in the PLR.

positive residuals of sequence B and negative residuals of sequence C′ have distinct truncations (top two panels (a) in Figure 6). As a result, these two sequences do not well satisfy a Gaussian distribution. Besides, due to small and more scattered samples, the symmetric distribution of the SMC O-rich AGB star sequences is weak.

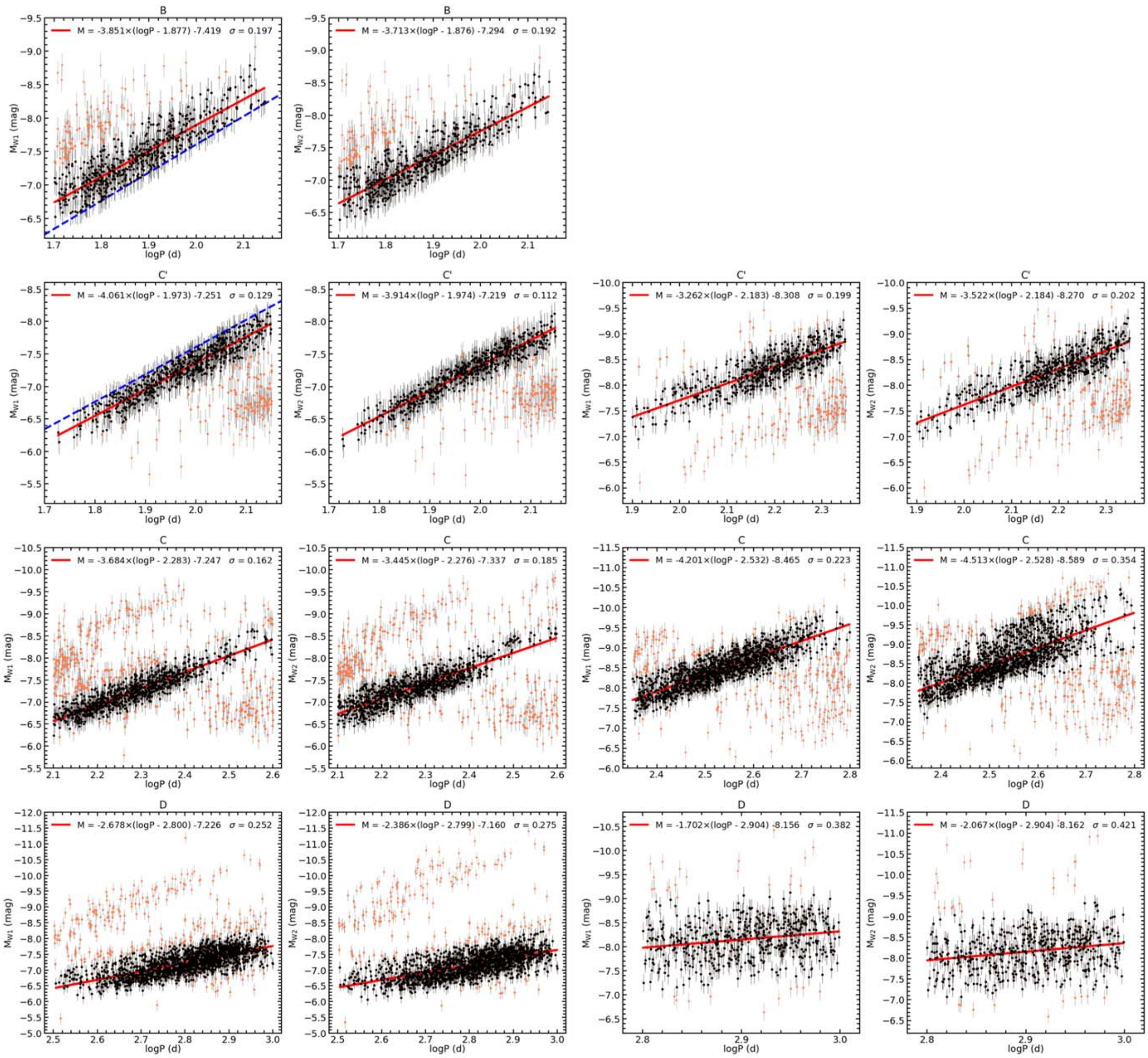

(a) O-rich AGB stars (b) C-rich AGB stars

Figure 4. PLRs of individual sequences in Figure 2 for AGB stars in LMC. Panel (a) shows the PLRs for O-rich AGB stars in each sequence (B_o, C'_o, C_o, D_o from top to bottom) in the W1 (left) and W2 (right) bands. Similar to panel (a), panel (b) is for C-rich AGB stars in sequences C'_c, C_c and D_c. The final LPVs with total absolute magnitude uncertainties $\sqrt{W}$ are plotted with black points. Stars rejected during the sigma-clipping procedure are plotted in coral. The best-fit PLRs are indicated by the red solid lines. Blue dashed lines represent the line K dividing sequence B and C' in Figure 3. σ means the dispersion of the fit.

4. Discussion

4.1. PLR Comparison

In Section 3.3, the PLRs of each sequence for O-rich and C-rich AGB stars in LMC and SMC were determined. In this section, we compare these PLRs in both W1 and W2 bands (see Figure 7). We find that for each sequence, the PLRs of LMC and SMC are consistent with each other. The period of sequence D is the LSP of AGB stars, and the PLR dispersion of sequence D is larger than the other sequences. This is understandable because the measurement precision is lower for the LSP. Soszyński et al. (2021) detected secondary eclipses in MIR light curves and argued that an eclipsing binary is a reasonable explanation for the origin of the LSP. In LMC and

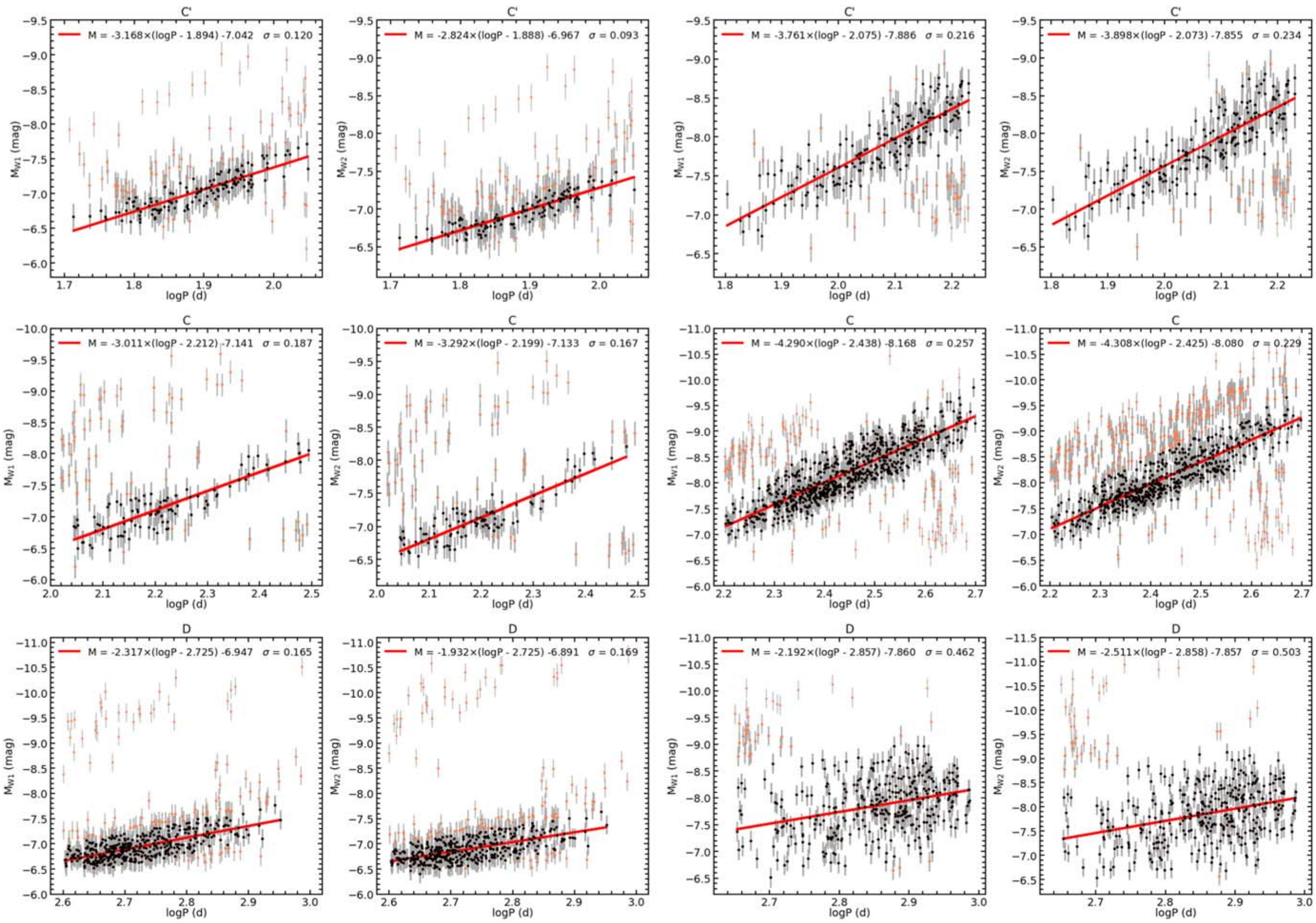

(a) O-rich AGB stars (b) C-rich AGB stars

Figure 5. Similar to Figure 4, but for the AGB stars in SMC. Panel (a) shows PLRs of the sequences C'_o, C_o, and D_o from top to bottom for O-rich AGB stars. Panel (b) shows PLRs of the sequences C'_c, C_c and D_c from top to bottom for C-rich AGB stars.

SMC, Soszyński et al. (2007) obtained the PLR of sequence D and found it to be a continuation of the PLR of sequence E at the bright end. Sequence E is predominantly a binary system of red giants. For contact binaries, there is a tight relationship between radius and orbital period due to the Roche lobe constraint, which allows the derivation of the infrared PLR. The infrared PLR is found for main sequence stars (Chen et al. 2018) and red giants (Muraveva et al. 2014) as components of contact binaries. Due to the consistency of the D and E sequences, PLR also exists for AGB contact binaries. When an AGB contact binary has not yet filled the two Roche lobes (detached or semi-detached binary), the orbital period is slightly larger, but the change in $\log P$ is small (<0.3), so the PLR still roughly holds. For AGB binaries with orbital periods twice as large, Gaia DR3 is unable to detect them. These reasons lead to the D sequence being a PLR with large dispersion.

Mira is a subtype of AGB stars with large amplitude in sequence C (Wood 2015). Iwanek et al. (2021b) determined the PLRs in the MIR bands based on Miras in LMC. We compared the PLRs of sequence C of AGB stars in LMC with the PLRs of Miras in Figure 8. For O-rich AGB stars and Miras, the PLRs are consistent. However, the PLR of C-rich AGB stars in the W2 band is slightly different from that of Miras. Miras show a brighter PLR with a steeper slope. After inspection, we found that the PLR of C-rich AGB stars with larger amplitudes in the C sequence is different from that of stars with smaller amplitudes. In contrast, this difference is negligible in the W1 band. We suspect that the difference in the W2-band PLR is due to the fact that large-amplitude C-rich AGB stars have more circumstellar dust, which enhances the dust emission in the W2 band. Trabucchi et al. (2021) also found these PLR features in SRVs. They found that the fundamental-mode SRVs are split into two branches, and those with relatively larger

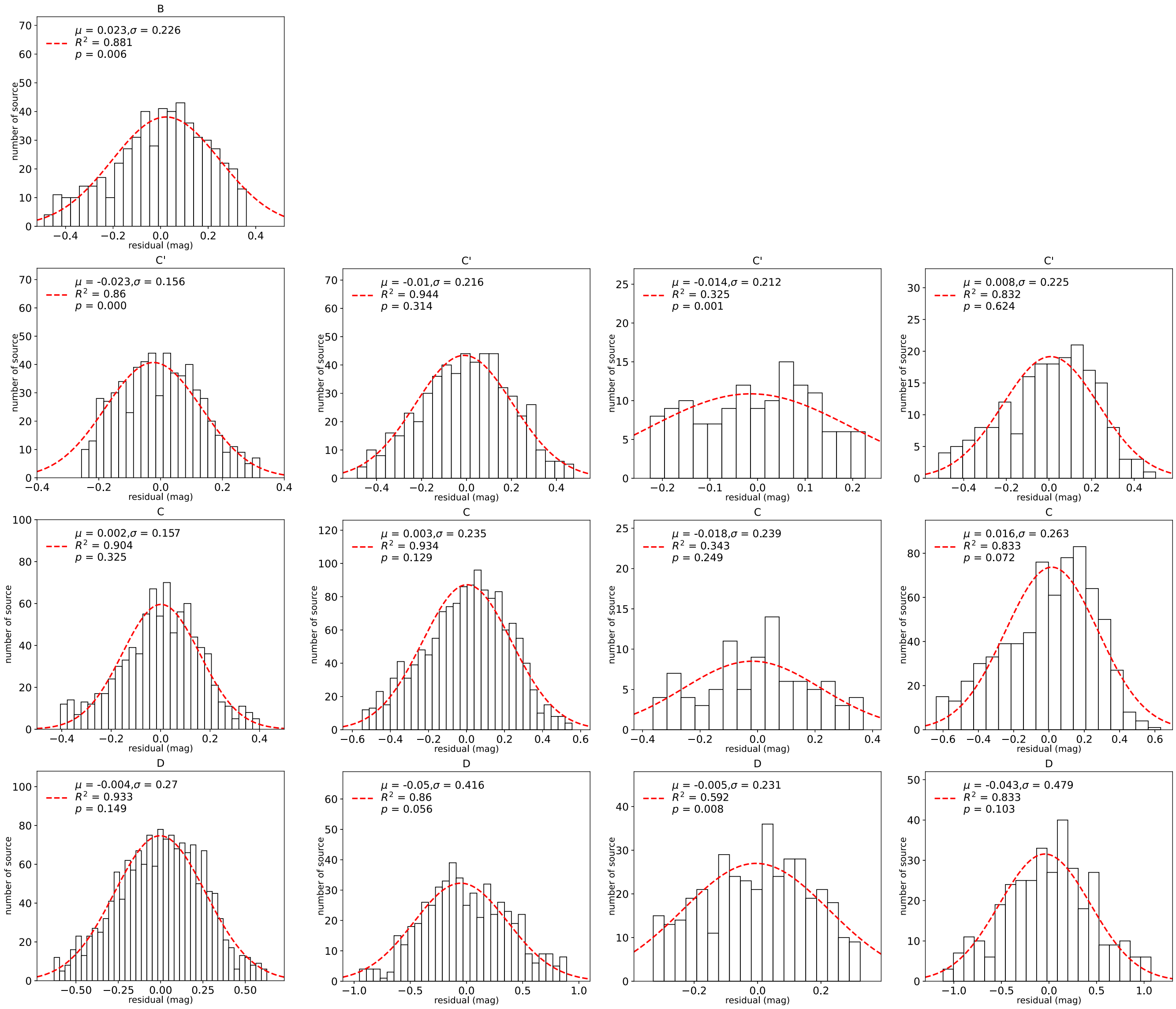

(a) LMC O-rich AGB stars (b) LMC C-rich AGB stars (c) SMC O-rich AGB stars (d) SMC C-rich AGB stars

Figure 6. Histogram of the magnitude differences from the best-fit line for each sequence of LMC and SMC AGB stars in W1 band. In each panel, the red dashed line shows the curve determined by a Gaussian fit. The μ and σ of the fitting curve are shown. Additionally, R^2 is displayed to imply the goodness of the fit. p-value represents the Gaussian distribution significance from the Kolmogorov–Smirnov test.

amplitudes satisfy the same distribution as Miras in the period–amplitude and PL diagrams.

4.2. The Dependence of PLRs on Metallicity

To check the correlation between the PLR zero-point and metallicity, we used metallicity ([M/H]) from Apache Point Observatory Galactic Evolution Experiment (APOGEE, Majewski et al. 2017) DR17. The metallicity was determined by the APOGEE Stellar Parameters and Abundances Pipeline (ASPCAP). In LMC, there are 87, 34, 30 and 98 O-rich AGB stars with metallicities in sequences B, C′, C and D, and 11, 39 and 5 C-rich AGB stars with metallicities in sequences C′, C and D, respectively. For SMC, sequence C′ contains only 5 O-rich and 6 C-rich AGB stars with metallicities, and sequence C contains 4 O-rich and 17 C-rich AGB stars with metallicities.

Figure 9 shows the distributions of carbon abundance and metallicity of AGB stars in LMC and SMC. We can see that there is a clear boundary between C-rich and O-rich AGB stars in the carbon abundance, which indicates that the classification of AGB stars using colors is appropriate. The metallicities of

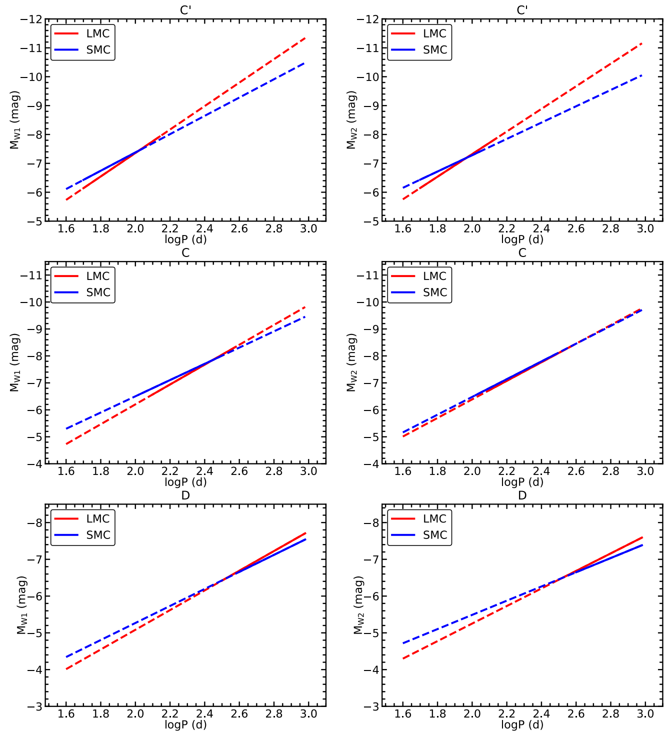

(a) O-rich AGB stars

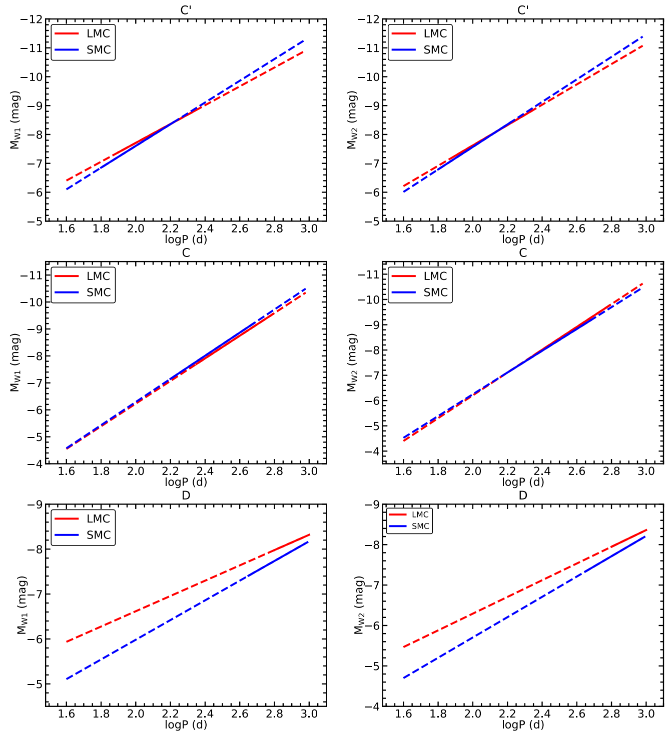

(b) C-rich AGB stars

Figure 7. Comparison of PLRs for the corresponding sequences (C′, C, and D from top to bottom) of AGB stars in LMC (red lines) and SMC (blue lines). Panel (a) shows the comparison of O-rich AGB stars, where the PLRs in the W1 band are displayed in the left column and in the W2 band in the right column. Similar to panel (a), panel (b) features the comparison of C-rich AGB stars from LMC and SMC. The solid lines indicate the PLR within the main period range of each sequence in the observations, and the dashed lines indicate the PLR at other periods. It should be noted that at other periods, AGB stars are not necessarily present.

O-rich AGB stars in SMC (red dots) are overall 0.2 dex poorer than those in LMC (green dots). The difference reflects the overall difference in metallicity between LMC and SMC. These imply that ASPCAP metallicities are suitable for internal comparison and statistical analysis. The metallicity of O-rich AGB stars in LMC ranges from −1.2 to −0.3 dex, while in SMC the metallicity ranges from −1.5 to −0.6 dex. Compared to O-rich AGB stars, the metallicity of C-rich AGB stars is much lower ([M/H] ∼ –2.0 dex), and metal-poor C-rich AGB stars are older stars with lower initial masses.

Considering the small sample size of C-rich AGB stars in LMC and O- and C-rich AGB stars in SMC, we focused only on the metallicity effect of O-rich AGB stars in LMC. We obtained the relations between the residuals and the metallicity. This method is more accurate than the three-parameter regression in cases where metallicity and period are not independent. Figure 10 shows the correlation between metallicities and the W1 and W2 band magnitude zero-point residuals of PLRs of sequences in LMC's O-rich AGB stars. The residuals are the observed absolute magnitudes minus the absolute magnitudes estimated by the PLRs in Table 1. We found that for O-rich AGB stars in LMC, there is a correlation between the PLR residuals and metallicities in each sequence. We fitted them with a linear relationship ($\Delta M_{\mathrm{W}} = \alpha + \beta \times$ [M/H]) using the weighted least squares method, where the weights are represented by $(\sigma_{\mathrm{M}}^2 + \sigma_{\mathrm{fit}}^2)^{-1}$. The metallicity effect of each sequence is listed in Table 3.

The metallicity effect of each sequence is similar between W1 and W2 bands, i.e., the sequence C′ has the lowest metallicity dependence while sequences C and D have the largest dependence. In particular, the metallicity dependence of sequence C′ in the W2 band is only about 0.8σ, which means that there is no obvious metallicity effect. However, based on non-zero coefficient of the metallicity effect (β = –0.746 ∼ –0.296 mag dex^{-1}) and significance of 2.2–3.5σ of four sequences in W1 band and 4.9σ of sequence C in W2 band, we suggest that the effect of metallicity may need to be taken into account in distance measurements with either O-rich AGB stars or Miras. At a fixed period, the luminosity of the O-rich AGB stars becomes brighter in the infrared bands when the metallicity increases. This trend is similar to that of classical Cepheids. For Cepheids, the luminosity also brightens with increasing metallicity for a given period (Riess et al. 2021).

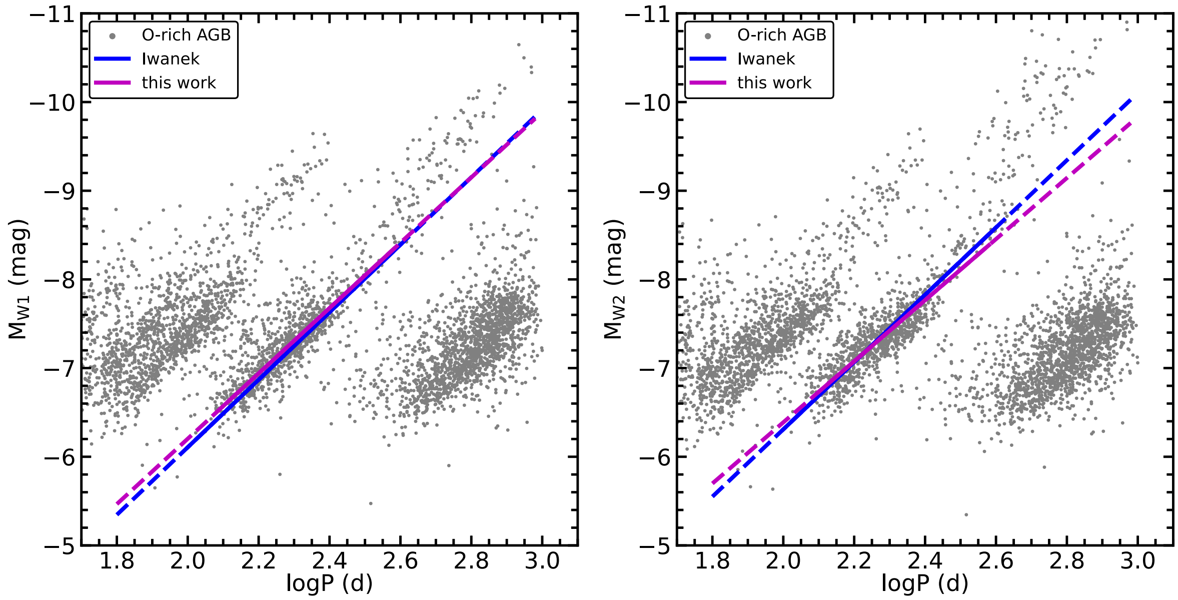

(a) O-rich AGB stars

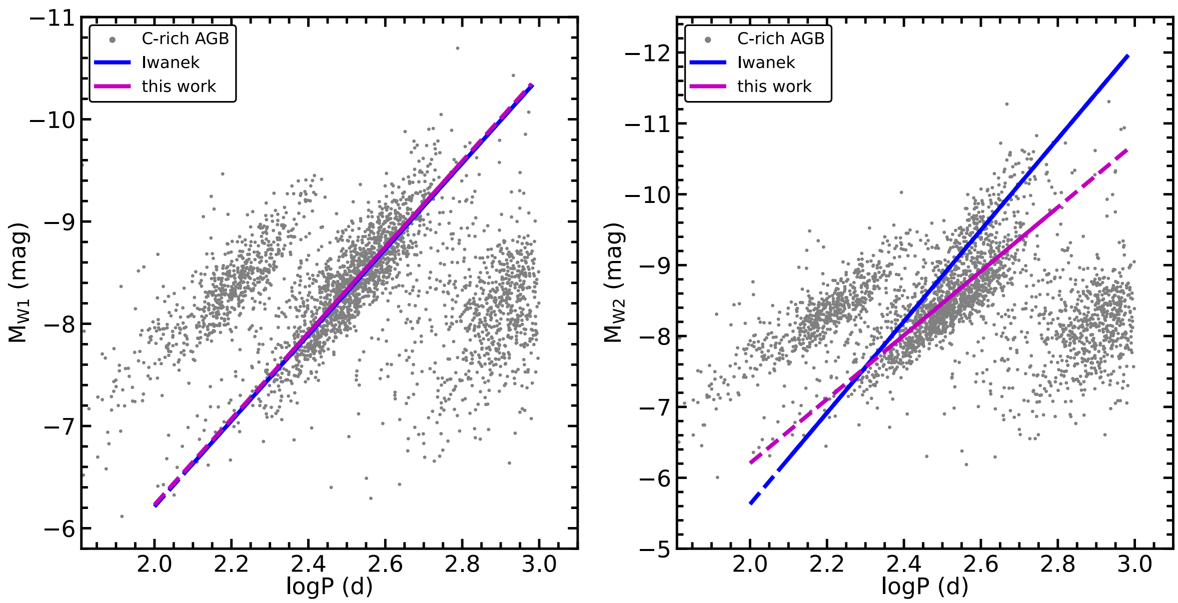

(b) C-rich AGB stars

Figure 8. Comparison of the PLRs between sequence C of AGB stars in this work and Miras from Iwanek et al. (2021b) in both the W1 and W2 bands. The gray dots indicate the O-rich (a) and C-rich (b) AGB stars in LMC. The magenta lines are the best-fitting PLRs of the sequence C of AGB stars in this work, and the blue lines represent the PLRs of Miras from Iwanek et al. (2021b). The dashed and solid lines are the same as in Figure 7.

To double-check the metallicity effect based on the same sample, we determined the period–luminosity–metallicity relation (PLMR) $M_{\rm W} = a_1 \times (\log P - \log P_0) + c_1 \times [{\rm M/H}] + b_1$, which includes metallicity as an independent parameter. For O-rich AGB stars in LMC, we performed the fit and tested the metallicity effect with a T-test. A smaller p-value of coefficient c_1 (p_{c_1}) indicates a more significant metallicity effect. The PLMRs and p_{c_1} of each sequence in both W1 and W2 bands are listed in

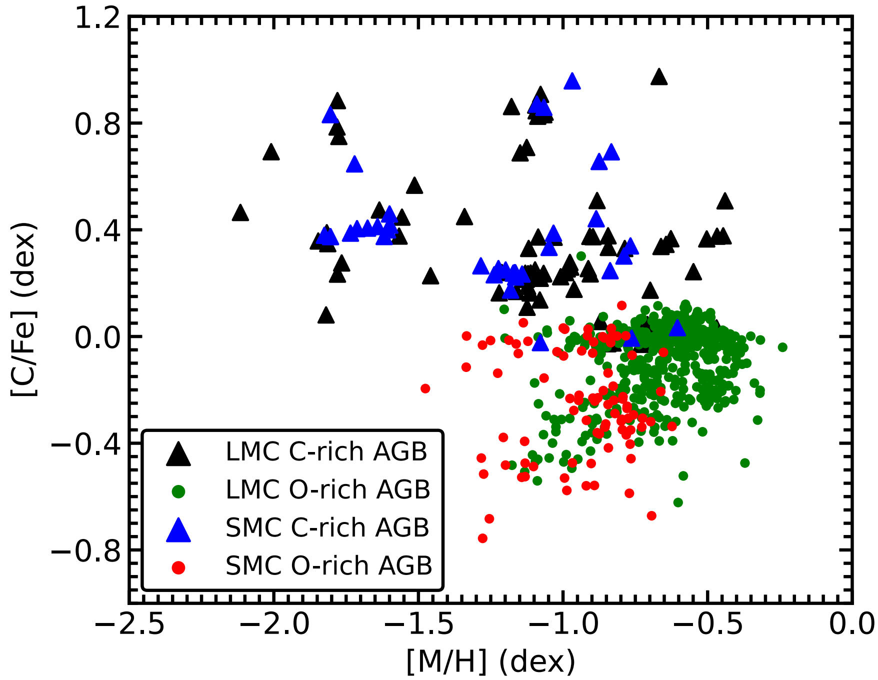

Figure 9. Carbon abundance against metallicity for AGB stars in LMC and SMC. Solid triangles represent C-rich AGB stars, while solid dots are the O-rich AGB stars.

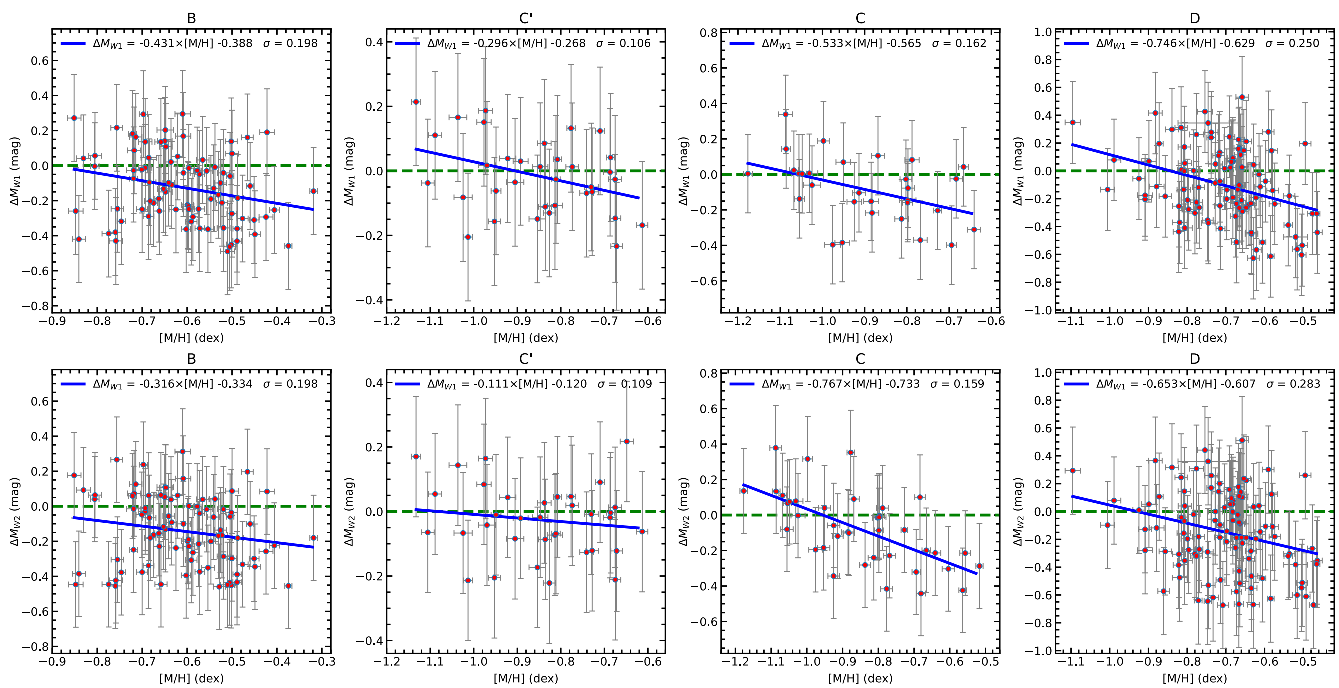

Figure 10. The dependence of PLR residuals of sequences for LMC's O-rich AGB stars (B, C′, C, D) on metallicities in the W1 (top panel) and W2 (bottom panel) band. The metallicity error and PLR residual uncertainty of each AGB star are indicated as gray error bars. In each panel, the green dashed line shows the zero line, while the blue solid line represents the linear fit between the PLR residuals and metallicities.

Table 3
Correlation Between PLRs and Metallicity of O-rich AGB Stars in LMC

Sequence	λ	α	β	σ_{fit}	λ	α	β	σ_{fit}
B ($1.7 \leqslant \log P \leqslant 2.13$)	W1	-0.388 ± 0.117	-0.431 ± 0.189	0.198	W2	-0.334 ± 0.117	-0.316 ± 0.188	0.198
C′ ($1.8 \leqslant \log P \leqslant 2.15$)	W1	-0.268 ± 0.118	-0.296 ± 0.136	0.106	W2	-0.120 ± 0.116	-0.111 ± 0.135	0.109
C ($2.1 \leqslant \log P \leqslant 2.5$)	W1	-0.565 ± 0.193	-0.533 ± 0.213	0.162	W2	-0.733 ± 0.137	-0.767 ± 0.158	0.159
D ($2.6 \leqslant \log P \leqslant 3.0$)	W1	-0.629 ± 0.152	-0.746 ± 0.213	0.250	W2	-0.607 ± 0.165	-0.653 ± 0.230	0.283

Note. The relationship between metallicity and magnitude residual of PLRs $\Delta M_{\mathrm{W}} = \alpha + \beta \times$ [M/H], where the ΔM_{W} is the observed absolute magnitude minus the absolute magnitude predicted by the PLRs in Table 1.

Table 4
PLRs and PLMRs for O-rich AGB Stars of LMC in Figure 10

Sequence	log P_0	a_1	b_1	c_1	σ_{fit}	p_{c_1}
			W1 band			
B ($1.70 \leqslant \log P \leqslant 2.13$)	1.877	-3.724 ± 0.232	-7.849 ± 0.139	-0.482 ± 0.211	0.197	0.025
C′ ($1.82 \leqslant \log P \leqslant 2.15$)	1.973	-4.362 ± 0.236	-7.434 ± 0.134	-0.199 ± 0.155	0.103	0.209
C ($2.11 \leqslant \log P \leqslant 2.56$)	2.283	-3.162 ± 0.271	-7.990 ± 0.207	-0.732 ± 0.228	0.152	0.003
D ($2.60 \leqslant \log P \leqslant 3.00$)	2.800	-2.360 ± 0.335	-7.963 ± 0.191	-0.880 ± 0.255	0.249	0.001
B ($1.70 \leqslant \log P \leqslant 2.13$)	1.877	-3.958 ± 0.214	-7.538 ± 0.027	⋯	0.203	⋯
C′ ($1.82 \leqslant \log P \leqslant 2.15$)	1.973	-4.511 ± 0.208	-7.265 ± 0.019	⋯	0.106	⋯
C ($2.11 \leqslant \log P \leqslant 2.56$)	2.283	-3.556 ± 0.279	-7.331 ± 0.034	⋯	0.178	⋯
D ($2.60 \leqslant \log P \leqslant 3.00$)	2.800	-2.999 ± 0.295	-7.314 ± 0.030	⋯	0.264	⋯
			W2 band			
B ($1.72 \leqslant \log P \leqslant 2.13$)	1.876	-3.714 ± 0.228	-7.628 ± 0.137	-0.316 ± 0.210	0.198	0.136
C′ ($1.82 \leqslant \log P \leqslant 2.15$)	1.974	-4.302 ± 0.234	-7.224 ± 0.133	0.024 ± 0.155	0.104	0.879
C ($2.11 \leqslant \log P \leqslant 2.54$)	2.276	-3.341 ± 0.244	-8.099 ± 0.153	-0.799 ± 0.175	0.158	0.001
D ($2.54 \leqslant \log P \leqslant 3.00$)	2.799	-1.873 ± 0.336	-7.945 ± 0.201	-0.877 ± 0.272	0.280	0.002
B ($1.72 \leqslant \log P \leqslant 2.13$)	1.876	-3.861 ± 0.207	-7.425 ± 0.026	⋯	0.200	⋯
C′ ($1.82 \leqslant \log P \leqslant 2.15$)	1.974	-4.283 ± 0.196	-7.244 ± 0.018	⋯	0.105	⋯
C ($2.11 \leqslant \log P \leqslant 2.54$)	2.276	-3.805 ± 0.275	-7.414 ± 0.033	⋯	0.199	⋯
D ($2.54 \leqslant \log P \leqslant 3.00$)	2.799	-2.459 ± 0.295	-7.303 ± 0.031	⋯	0.294	⋯

Note. PLRs and PLMRs of samples in Figure 10 in W1 and W2 bands. The PLR slope a_1 and the zero-point b_1 are determined from the linear fit based on $M_{\mathrm{W}} = a_1 \times (\log P - \log P_0) + b_1$, where the value of $\log P_0$ is same as that in Table 1. The PLMR slope a_1, metallicity coefficient c_1 and zero-point b_1 are determined from the linear fit based on $M_{\mathrm{W}} = a_1 \times (\log P - \log P_0) + c_1 \times$ [M/H] $+ b_1$, where the $c_1 \times$ [M/H] is the metallicity term. σ_{fit} means the 1σ scatter in the PLMR. p_{c_1} is the p-value of c_1 from T-test. A smaller p_{c_1} indicates a more significant metallicity effect.

Table 4. Similarly, the metallicity effect is significant (2σ) except for the sequence C′ in W1 band, and sequences B and C′ in W2 band.

In addition, we obtained the PLR $M_{\mathrm{W}} = a_1 \times (\log P - \log P_0) + b_1$ for the same sample. We found that the PLR scatter of each sequence is larger than that of PLMR by 1% −20%. Considering that the main components in the PLR dispersion (0.1−0.2 mag) come from the dispersion introduced by period errors and the intrinsic PLR dispersion, which are not reduced by the inclusion of the metallicity term, the optimization of the other dispersion is greater than 1%–20% with the inclusion of the metallicity term. The results are shown in Table 4. Both methods suggest that for O-rich AGB stars, metallicity effect in the PLR may need to be considered.

After APOGEE DR16, the accuracy and consistency of stellar parameters for cool stars ($T_{\mathrm{eff}} < 3500$ K) are improved due to the use of MARCS model atmospheres in spherical symmetry (Schultheis et al. 2020). To double-check the reliability of the ASPCAP metallicities of AGB stars, we compared them with those obtained from the Brussels Automatic Code for Characterizing High-accUracy Spectra (BACCHUS). The BACCHUS Analysis of Weak Lines in APOGEE Spectra (BAWLAS, Hayes et al. 2022) catalog includes the chemical abundances of about 120,000 giants with

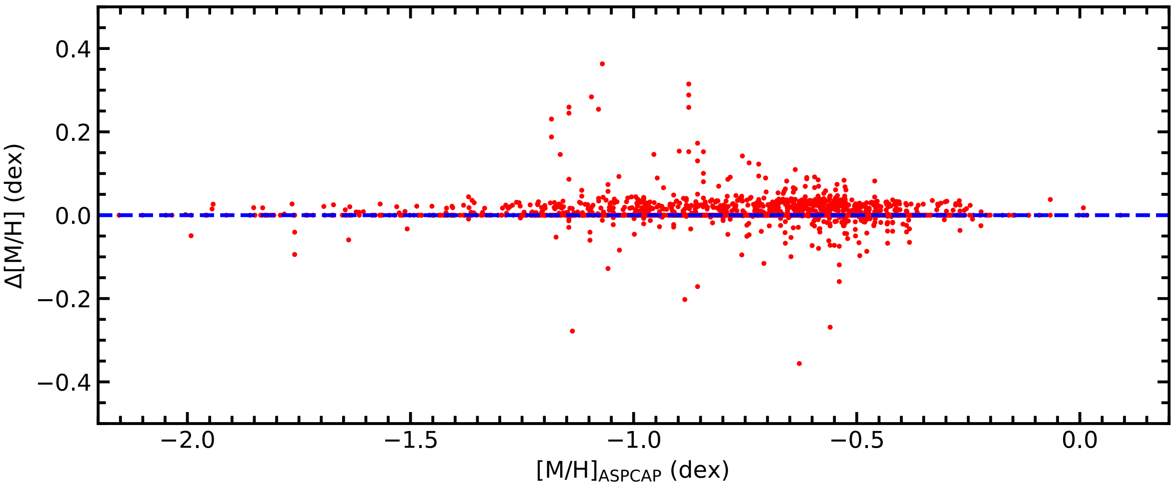

Figure 11. The comparison of ASPCAP and BAWLAS metallicity for AGB stars. Δ[M/H] is the BAWLAS metallicity minus the ASPCAP metallicity. $[M/H]_{ASPCAP}$ represents the metallicity from ASPCAP. The blue dashed line is the zero line.

APOGEE DR17 spectra. We used 1″ to cross-match our AGB stars with objects from the BAWLAS catalog and obtained 1869 AGB stars with both the ASPCAP and BAWLAS metallicities. The comparison of the metallicities of these AGB stars is shown in Figure 11. We found that 94.7% of AGB stars have a metallicity difference smaller than 0.05 dex. The overall bias is $\Delta[M/H] = 0.007 \pm 0.033$ dex. This means that the metallicity of ASPCAP is reliable for AGB stars, at least suitable for internal comparisons and statistical analysis.

5. Conclusion

We analyzed the MIR PLRs of LPVs in LMC and SMC using the Gaia DR3 LPVs and the WISE database. For LMC and SMC, LPV candidates were selected by considering their positions in the sky. Meanwhile, we excluded LPVs affected by other sources by the blending factor larger than 1.05 in *K*-band. Finally, we cross-matched them with the AllWISE and NEOWISE databases and obtained their photometric data in MIR. Based on fitting the light curves, the mean magnitudes of these objects are determined. The LPVs are classified into AGB, RGB, and RSG stars according to their positions on the CMDs ($W_{BP,RP}$ versus $G_{BP} - G_{RP}$). In this work we focused on AGB stars, which account for most of the LPVs. AGB stars are further classified as C-rich and O-rich subtypes according to the parameter in the Gaia DR3 LPV catalog. In the PL diagrams (M_{W1} versus $\log P$), O-rich and C-rich AGB stars in LMC show four and three distinct sequences, respectively. For SMC, there are three sequences for both O-rich and C-rich AGB stars. We used the weighted least squares method to obtain the best-fit linear PLR for each sequence of LMC and SMC as well as its uncertainty.

We compared the PLRs in the W1 and W2 bands for each sequence of LMC and SMC. The PLRs of the O-rich AGB stars in sequences C′ and C have smaller dispersion, and they are more suitable as distance indicators. The dispersion of the D-sequence PLR is larger, due to the less accurate measurement of the LSP. The PLRs of LMC and SMC AGB stars in each sequence are very consistent, especially for sequence C. We compared the PLRs of C-sequence AGB stars in LMC with the PLRs of Miras in the literature and found that the PLRs of O-rich AGB stars and O-rich Miras are consistent. However, the PLRs of C-rich AGB stars and C-rich Miras in sequence C have significant differences in the W2 band. The W2-band PLR of C-rich Miras is brighter and has a steeper slope. This is due to the fact that the large-amplitude C-rich AGB stars have more circumstellar dust, leading to an excess in the MIR bands.

We investigated the dependence of PLRs on metallicity ([M/H]) for LMC O-rich AGB stars and found linear relations ($\sigma = 2.3-4.9$) between the PLR zero-point residuals and metallicities for sequences B, C and D in W1 band and sequences C and D in W2 band. The coefficients of the metallicity effect are $\beta = -0.533 \pm 0.213$ mag dex^{-1} and $\beta = -0.767 \pm 0.158$ mag dex^{-1} for sequence C in W1 and W2 bands, respectively. We also found that the scatter in PLMR is smaller than PLR based on the same sample, and the *p*-value indicates a significant relationship with metallicity ($\sigma = 2.3-4.6$) for PLMR in sequences B, C and D in W1 band, and sequences C and D in W2 band. We suggest that the metallicity effect may need to be taken into account when measuring distances using O-rich Miras or O-rich AGB stars. Based on future APOGEE data, the coefficient error of the metallicity effect will be optimized to a level of 0.05−0.10 mag dex^{-1}.

Acknowledgments

We thank the anonymous reviewer for the comments. This work was supported by the National Natural Science Foundation of China (NSFC, Grant Nos. 12173047, 12322306, 12003046, 12233009, and 12133002). X.C. and S.W. acknowledge support from the Youth Innovation Promotion Association of the Chinese Academy of Sciences (no. 2022055 and 2023065). We are also thankful for the support from the National Key Research and Development Program of China, grants 2022YFF0503404 and 2019YFA0405504. This publication makes use of data products from AllWISE and NEOWISE, which are projects of the Jet Propulsion Laboratory/California Institute of Technology. AllWISE and NEOWISE are funded by the National Aeronautics and Space Administration. This work presents results from the European Space Agency (ESA) space mission Gaia. Gaia data are being processed by the Gaia Data Processing and Analysis Consortium (DPAC). Funding for the DPAC is provided by national institutions, in particular the institutions participating in the Gaia MultiLateral Agreement (MLA). The Gaia mission website is https://www.cosmos.esa.int/gaia. The Gaia archive website is https://archives.esac.esa.int/gaia. APOGEE survey is part of Sloan Digital Sky Survey (SDSS) IV. SDSS-IV acknowledges support and resources from the Center for High Performance Computing at the University of Utah. SDSS-IV is managed by the Astrophysical Research Consortium for the Participating Institutions of the SDSS Collaboration (https://www.sdss.org).

ORCID iDs

Xiaodian Chen https://orcid.org/0000-0001-7084-0484
Shu Wang https://orcid.org/0000-0003-4489-9794

References

Bhardwaj, A., Kanbur, S., He, S., et al. 2019, ApJ, 884, 20
Boyer, M. L., Srinivasan, S., van Loon, J. T., et al. 2011, AJ, 142, 103
Chen, X., Deng, L., de Grijs, R., Wang, S., & Feng, Y. 2018, ApJ, 859, 140
Chen, X., Wang, S., Deng, L., et al. 2020, ApJS, 249, 18
Cook, K. H., Alcock, C., Allsman, R. A., et al. 1996, in Proc. of the 12th IAP Astrophysics Colloquium, Variable Stars and the Astrophysical Returns of Microlensing Surveys, ed. R. Ferlet, J.-P. Maillard, & B. Raban (Gif-sur-Yvetle Cedex: Editions Frontieres), 17
de Grijs, R., Courbin, F., Martínez-Vázquez, C. E., et al. 2017, SSRv, 212, 1743
Freedman, W. L., Madore, B. F., Hatt, D., et al. 2019, ApJ, 882, 34
Goldman, S. R., Boyer, M. L., McQuinn, K. B. W., et al. 2019, ApJ, 877, 49
Groenewegen, M. A. T. 2022, A&A, 659, A145
Hayes, C. R., Masseron, T., Sobeck, J., et al. 2022, ApJS, 262, 34
Huang, C. D., Riess, A. G., Hoffmann, S. L., et al. 2018, ApJ, 857, 67
Huang, C. D., Riess, A. G., Yuan, W., et al. 2020, ApJ, 889, 5
Ita, Y., Tanabé, T., Matsunaga, N., et al. 2004, MNRAS, 353, 705
Iwanek, P., Kozłowski, S., Gromadzki, M., et al. 2021a, ApJS, 257, 23
Iwanek, P., Poleski, R., Kozłowski, S., et al. 2023, ApJS, 264, 20
Iwanek, P., Soszyński, I., & Kozłowski, S. 2021b, ApJ, 919, 99
Kudashkina, L. S. 2019, Ap, 62, 556
Lebzelter, T., Mowlavi, N., Lecoeur-Taibi, I., et al. 2022, A&A, 674, 36
Majewski, S. R., Schiavon, R. P., Frinchaboy, P. M., et al. 2017, AJ, 154, 94
Matsunaga, N., Fukushi, H., & Nakada, Y. 2005, MNRAS, 364, 117
Menzies, J. W., Whitelock, P. A., Feast, M. W., & Matsunaga, N. 2019, MNRAS, 483, 5150
Molina, C. N., Borissova, J., Catelan, M., et al. 2019, MNRAS, 482, 5567
Mowlavi, N., Lecoeur-Taïbi, I., Lebzelter, T., et al. 2018, A&A, 618, A58
Mowlavi, N., Trabucchi, M., & Lebzelter, T. 2019, in 53rd ESLAB Symp., The Gaia Universe, 62
Muraveva, T., Clementini, G., Maceroni, C., et al. 2014, MNRAS, 443, 432
Parto, T., Dehghani, S., Javadi, A., et al. 2023, ApJ, 942, 33
Qin, W., Nataf, D. M., Zakamska, N., Wood, P. R., & Casagrande, L. 2018, ApJ, 865, 47
Riess, A. G., Casertano, S., Yuan, W., et al. 2021, ApJL, 908, L6
Saremi, E., Javadi, A., van Loon, J. T., et al. 2020, ApJ, 894, 135
Schultheis, M., Rojas-Arriagada, A., Cunha, K., et al. 2020, A&A, 642, A81
Soszyński, I., Dziembowski, W. A., Udalski, A., et al. 2007, AcA, 57, 201
Soszyński, I., Olechowska, A., Ratajczak, M., et al. 2021, ApJL, 911, L22
Soszyński, I., Udalski, A., Kubiak, M., et al. 2004, AcA, 54, 129
Soszyński, I., Udalski, A., Kubiak, M., et al. 2005, AcA, 55, 331
Spano, M., Mowlavi, N., Eyer, L., et al. 2011, A&A, 536, A60
Suh, K.-W. 2022, JKAS, 55, 195
Trabucchi, M., Mowlavi, N., & Lebzelter, T. 2021, A&A, 656, A66
Trabucchi, M., Wood, P. R., Montalbán, J., et al. 2017, ApJ, 847, 139
Urago, R., Omodaka, T., Nagayama, T., et al. 2020, ApJ, 891, 50
Van Eck, S., Neyskens, P., Jorissen, A., et al. 2017, A&A, 601, A10
Whitelock, P. A., Feast, M. W., & Van Leeuwen, F. 2008, MNRAS, 386, 313
Wiśniewski, M., Marquette, J. B., Beaulieu, J. P., et al. 2011, A&A, 530, A8
Wood, P. R. 2000, PASA, 17, 18
Wood, P. R. 2015, MNRAS, 448, 3829
Wood, P. R., Alcock, C., Allsman, R. A., et al. 1999, in IAU Symp. #191, Asymptotic Giant Branch Stars, ed. T. Le Bertre, A. Lebre, & C. Waelkens (San Francisco: Astronomical Soc Pacific), 151
Yuan, W., Macri, L. M., He, S., et al. 2017, AJ, 154, 149